
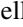





Spectral properties of the critical (1+1)-dimensional Abelian-Higgs model

Titas Chanda ^{1,2,*}, Marcello Dalmonte ^{2,3}, Maciej Lewenstein ^{4,5}, Jakub Zakrzewski ^{6,7} and Luca Tagliacozzo ^{8,†}

¹Department of Physics, Indian Institute of Technology Indore, Khandwa Road, Simrol, Indore 453552, India

²The Abdus Salam International Centre for Theoretical Physics (ICTP), Strada Costiera 11, 34151 Trieste, Italy

³International School for Advanced Studies (SISSA), via Bonomea 265, 34136 Trieste, Italy

⁴ICFO-Institut de Ciències Fotòniques, The Barcelona Institute of Science and Technology, Av. Carl Friedrich Gauss 3, 08860 Barcelona, Spain

⁵ICREA, Passeig Lluis Companys 23, 08010 Barcelona, Spain

⁶Instytut Fizyki Teoretycznej, Uniwersytet Jagielloński, Łojasiewicza 11, 30-348 Kraków, Poland

⁷Mark Kac Complex Systems Research Center, Jagiellonian University in Krakow, Łojasiewicza 11, 30-348 Kraków, Poland

⁸Instituto de Física Fundamental IFF-CSIC, Calle Serrano 113b, Madrid 28006, Spain



(Received 5 August 2023; revised 6 December 2023; accepted 7 December 2023; published 2 January 2024)

The presence of gauge symmetry in 1+1 dimensions is known to be redundant, since it does not imply the existence of dynamical gauge bosons. As a consequence, in the continuum, the Abelian-Higgs model (i.e., the theory of bosonic matter interacting with photons) just possesses a single phase, as the higher-dimensional Higgs and Coulomb phases are connected via nonperturbative effects. However, recent research published in [Phys. Rev. Lett. **128**, 090601 \(2022\)](#) has revealed an unexpected phase transition when the system is discretized on the lattice. This transition is described by a conformal field theory with a central charge of $c = 3/2$. In this paper, we aim to characterize the two components of this $c = 3/2$ theory—namely the free Majorana fermionic and bosonic parts—through equilibrium and out-of-equilibrium spectral analyses.

DOI: [10.1103/PhysRevB.109.045103](https://doi.org/10.1103/PhysRevB.109.045103)

I. INTRODUCTION

A physical theory is most often characterized by fixing its symmetries, the dimensions of space-time on which it operates, and its field content [1–5]. This concept forms the basis of the renormalization-group construction and our efforts to categorize its fixed points [6–10]. For instance, in a four-dimensional space-time, in a system featuring $U(1)$ gauge-invariance and fermionic matter, we expect the physics to be described by quantum electrodynamics, where the fermions correspond to electrons and the gauge bosons correspond to photons [11,12].

Here we analyze a scenario that shows that this simple picture does not necessarily hold. The lattice discretization of the Abelian-Higgs model [11–16] (see Refs. [17–25] for recent discussions on realizing the Abelian-Higgs model in quantum simulators), defined on one spatial and one time dimension (1+1D), shares the same dimensionality and field content with the same in the continuum. However, as shown recently in Ref. [26], strong correlations induce an emergent physical theory on the lattice that can be described, at low energies, as one massless relativistic fermion together with a massless relativistic boson.

The Abelian-Higgs model is among the simplest $U(1)$ gauge theories in 1+1D. It contains bosonic matter (the Higgs part of the model) and constitutes a well-known

textbook example of gauge theory [11,12,27]. The model is described by the action [with the metric convention $g_{\mu\nu} = \text{diag}(-1, 1)$]

$$S = \int d^2x \left(-\frac{1}{2} F^{01} F_{01} - D^v \phi (D_v \phi)^* - m^2 |\phi|^2 - \frac{\lambda}{2} |\phi|^4 + \frac{\theta}{2\pi} q F^{01} \right), \quad (1)$$

where $D_v = \partial_v + iqA_v$ is the covariant derivative, with q being the charge of the scalar matter field described by the complex-valued field ϕ . m and λ are the bare mass and self-interaction of the scalar field, respectively, and θ is a periodic parameter, $-\pi \leq \theta \leq \pi$, that controls the background field.

Despite the similarity of the above action with higher-dimensional Abelian-Higgs models, the physics in 1+1D is very different [1,27,28]. In higher dimensions, the model displays two well-known phases, namely a Coulomb phase described by massless photons interacting with the matter field, and a Higgs phase where the photons are screened and acquire mass, and the Higgs field condenses [29,30]. In 1+1D, for positive m^2 the scalar matter is confined. Differently from the higher-dimensional models, instanton effects lead to confinement also for large and negative m^2 , destroying the expected screening caused by the condensation of the Higgs field [1,27,28]. The only exception to this simple scenario involving the occurrence of a single gapped phase in the continuum is at $\theta = \pi$ (see, e.g., [27,31–34]), where there is a line of first-order transition that culminates in a

*titas.hri@gmail.com

†luca.tagliacozzo@iff.csic.es

second-order critical point in the Ising universality class (akin to what happens in the Schwinger model [35,36]).

In recent works [26,37], the same model has been discretized on the lattice in the Hamiltonian formalism. Having L sites (with lattice spacing a) and $L - 1$ bonds, the corresponding Hamiltonian, at $\theta = 0$, reads

$$\hat{H} = \sum_j \left[\hat{L}_j^2 + 2x \hat{\Pi}_j^\dagger \hat{\Pi}_j + \left(4x - \frac{2\mu^2}{q^2} \right) \hat{\phi}_j^\dagger \hat{\phi}_j + \frac{\lambda}{q^2} (\hat{\phi}_j^\dagger)^2 \hat{\phi}_j^2 - 2x (\hat{\phi}_{j+1}^\dagger \hat{U}_j \hat{\phi}_j + \text{H.c.}) \right], \quad (2)$$

with $x = 1/a^2 q^2$ and $\mu^2 = -m^2$. The matter field operators, $\{\hat{\phi}_j, \hat{\phi}_j^\dagger, \hat{\Pi}_j, \hat{\Pi}_j^\dagger\}$, act on the Hilbert space at site j , while the gauge-field operators, $\{\hat{L}_j, \hat{U}_j, \hat{U}_j^\dagger\}$, act on the Hilbert space defined on the bond linking sites j and $j + 1$. The operators fulfill the standard canonical commutation relations:

$$\begin{aligned} [\hat{\phi}_j, \hat{\Pi}_k] &= [\hat{\phi}_j^\dagger, \hat{\Pi}_k^\dagger] = i\delta_{jk}, \\ [\hat{L}_j, \hat{U}_j] &= -\hat{U}_j, \quad [\hat{L}_j, \hat{U}_j^\dagger] = \hat{U}_j^\dagger. \end{aligned} \quad (3)$$

The usual continuum limit is taken as $x \rightarrow \infty$.

Rather than considering the usual continuum limit, $x = 2$ was fixed in [26], and the phase diagram as a function of λ and μ was characterized numerically with matrix product state (MPS) techniques [38,39] (see Refs. [40–50] for recent applications of MPS techniques in models of lattice gauge theory). On the lattice, the model presents a rich phase diagram. Even at $\theta = 0$, there is a first-order phase transition between two distinct regimes, a confined regime characterized by the suppression of the kinetic term of the Hamiltonian ($\hat{\phi}_{j+1}^\dagger \hat{U}_j \hat{\phi}_j + \text{H.c.}$) and low entanglement entropy in the ground state, and a gapped ‘‘Higgs’’ regime, characterized by a larger (but finite) kinetic energy and entanglement entropy. The first-order line ends in a second-order critical point. This critical point is described by a conformal field theory (CFT) with a central charge of $c = 3/2$. This implies that the interplay of lattice effects and nonperturbative physics can give rise to new emerging phenomena, whose field theory description is completely different from the original continuum field theory discretized to obtain the lattice model.

As a result, in the continuum we have two completely different models emerging from the same microscopic model. A gapped model of confined bosonic charges is obtained by taking $x \rightarrow \infty$ in any region of the phase diagram on the lattice model whose physics is well known and described in textbooks [11,12,27]. At the critical point on the lattice, however, we can take a different continuum limit at fixed x and obtain a gapless conformal field theory with $c = 3/2$ that originates from the same microscopic model—relativistic bosons interacting with a $U(1)$ gauge field. This continuum theory is less understood.

In this work, we proceed to better characterize this lattice microscopic model. We start by solving some of the puzzles presented in Ref. [26]. In particular, we show that all Renyi entropies, differently from what was claimed originally, scale as expected from the conformal field theory predictions once the subleading corrections are taken into account.

We then extract the sound velocity and the dispersion relation of the system via real-time dynamics, and we combine those with an accurate finite-size-scaling analysis of the Hamiltonian spectrum. From those, we identify the presence of a charge gap, and the portion of the low-energy spectrum that is responsible for critical behavior. Since the model is gauge-invariant, we can target different background charge sectors. In the zero background charge sector, we only find the Majorana fermionic or Ising part of the spectrum. On the other hand, using the known relation about the fluctuations of the charges, we also identify the value of the Luttinger liquid parameter of the bosonic sector of the theory.

The resulting picture is thus much clearer than before but still incomplete. The critical point of the discretized Abelian Higgs model in 1+1D provides an example of a relativistic CFT where a discrepancy between the scaling of entanglement and the low-energy spectrum is observed.

We thus extend our analysis to the other sectors of background charges, where we find many low-energy excitations that should encode the bosonic part of the spectrum. However, with our current tools we have limited precision in extracting the spectra in the other background charge sectors to properly identify all of them. Thus we are still not able to completely identify the full low-energy spectrum, something we plan to do in the future.

II. A BRIEF RECAP: THE SYSTEM

The Abelian-Higgs model in 1+1D is described by the Hamiltonian (2). We can then define creation and annihilation operators for particles ‘‘ a ’’ and antiparticles ‘‘ b ’’ as \hat{a}_j and \hat{b}_j , fulfilling $[\hat{a}_j, \hat{a}_k^\dagger] = [\hat{b}_j, \hat{b}_k^\dagger] = \delta_{jk}$. The operators are defined as

$$\begin{aligned} \hat{\phi}_j &= \frac{1}{\sqrt{2}}(\hat{a}_j + \hat{b}_j^\dagger), \quad \hat{\Pi}_j = \frac{i}{\sqrt{2}}(\hat{a}_j^\dagger - \hat{b}_j), \\ \hat{\phi}_j^\dagger &= \frac{1}{\sqrt{2}}(\hat{a}_j^\dagger + \hat{b}_j), \quad \hat{\Pi}_j^\dagger = \frac{i}{\sqrt{2}}(\hat{b}_j^\dagger - \hat{a}_j), \end{aligned}$$

as discussed in, e.g., [37].

A. Gauge invariance and Gauss law generators

In the absence of external charges, the local $U(1)$ symmetry implies that all physical states $|\Psi\rangle$ satisfy the Gauss law $\hat{G}_j|\Psi\rangle = 0$, $\forall j$, where the generators are [37]

$$\hat{G}_j = \hat{L}_j - \hat{L}_{j-1} - \hat{Q}_j, \quad (4)$$

with $\hat{Q}_j = \hat{a}_j^\dagger \hat{a}_j - \hat{b}_j^\dagger \hat{b}_j$ describing the dynamical charge. Using the Gauss law, we can integrate out the gauge fields in a chain with open boundary conditions by the nonlocal transformations

$$\left(\prod_{l \leq j} \hat{U}_l \right) \hat{\phi}_j \rightarrow \hat{\phi}_j, \quad \left(\prod_{l \leq j} \hat{U}_l^\dagger \right) \hat{\Pi}_j \rightarrow \hat{\Pi}_j, \quad \hat{L}_j = \sum_{l \leq j} \hat{Q}_l. \quad (5)$$

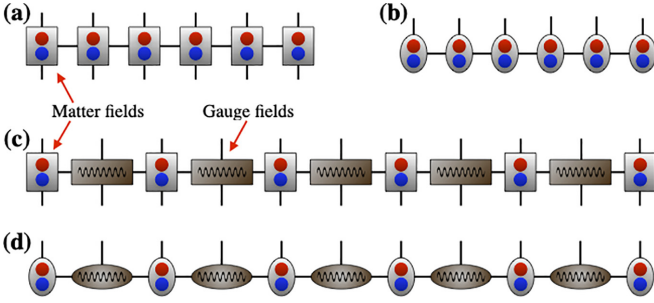


FIG. 1. Diagrammatic depictions of the MPO [panels (a) and (c)] and MPS [panels (b) and (d)] representations used in this paper. Panels (a) and (b) correspond to the long-range matter-only description of Eq. (6), while (c) and (d) presents the same for the matter-gauge picture of Eq. (2).

This introduces a long-range potential for the matter fields [51] as follows:

$$\hat{H} = \sum_j \left[\left(\sum_{l \leq j} \hat{Q}_l \right)^2 + 2x \hat{\Pi}_j^\dagger \hat{\Pi}_j + \left(4x - \frac{2\mu^2}{q^2} \right) \hat{\phi}_j^\dagger \hat{\phi}_j + \frac{\lambda}{q^2} (\hat{\phi}_j^\dagger)^2 \hat{\phi}_j^2 - 2x (\hat{\phi}_{j+1}^\dagger \hat{\phi}_j + \text{H.c.}) \right]. \quad (6)$$

In the rest of the paper, unless explicitly stated otherwise, we shall consider Eq. (6) as the system Hamiltonian that respects global $U(1)$ symmetry corresponding to the conservation of the total dynamical charge $\hat{Q} = \sum_j \hat{Q}_j$. [It should be noted that since the mapping in Eq. (5) is exact, the long-range Hamiltonian (6) describes the same physics as that of the short-range matter-gauge Hamiltonian (2). We verify this numerically in Appendix B.] We use the density matrix renormalization group (DMRG) algorithm [38,39,52–55] in the framework of the matrix product states (MPSs) to find the ground state or low-lying excited states of the Hamiltonian (6). The diagrammatic depictions of the matrix product operator (MPO) for the Hamiltonian (6) and the corresponding MPSs are given in Figs. 1(a) and 1(b), respectively. In Figs. 1(c) and 1(d), we also present the same for the short-range matter-gauge description of Eq. (2), where we also impose global $U(1)$ symmetry to conserve the total dynamical charge \hat{Q} . For time-evolution, we use the MPS-based time-dependent variational principle (TDVP) [56–59] concentrating only on the long-range description.

B. The phase diagram

The phase diagram of the Abelian-Higgs model in 1+1D on a discrete lattice has been studied recently in [26]. Here we present a different characterization leading to the same phase-diagram. In continuum, the phase diagram of the Abelian-Higgs model is somewhat uninteresting as there exists only one gapped confined phase without any phase transition in the absence of a background field. However, the lattice discretization unveils a rich landscape of phase transitions between the confined and the Higgs phase. At weak coupling (i.e., at small λ/q^2) these two phases are separated by a line of first-order quantum phase transitions (FOQPTs)

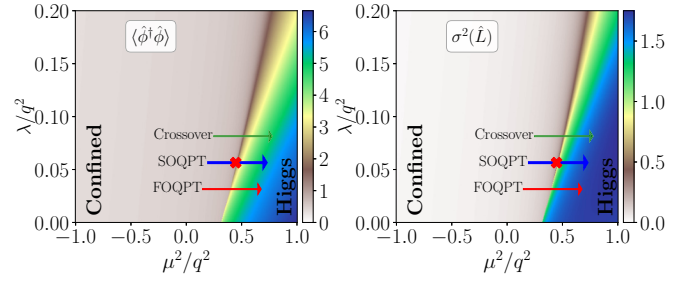


FIG. 2. Phase diagram of the Abelian-Higgs model in 1+1D (6) in the $(\mu^2/q^2, \lambda/q^2)$ -plane for a system of size $L = 60$. The left panel shows the behavior of the expectation value $\langle \hat{\phi}^\dagger \hat{\phi} \rangle$, while the right panel is for the variance $\sigma^2(\hat{L})$. Both quantities are averaged over lattice sites/bonds.

that ends at a critical second-order quantum phase transition (SOQPT). Above this SOQPT point, these two phases are smoothly connected by a crossover. In Fig. 2, we depict the phase diagram of the system in the $(\mu^2/q^2, \lambda/q^2)$ -plane.

In the Higgs phase, since the gauge field becomes massive, its quantum fluctuations as measured by the variance $\sigma^2(\hat{L}_j) = \langle \hat{L}_j^2 \rangle - \langle \hat{L}_j \rangle^2$ becomes nonzero, while it remains vanishingly small in the confined region. In contrast, since the matter field attains a finite expectation value in the Higgs phase, $\langle \hat{\phi}_j^\dagger \hat{\phi}_j \rangle$ becomes large, as seen in Fig. 2.

The SOQPT point has been located precisely to be $[\lambda_c/q^2 = 0.0565(1), \mu_c^2/q^2 = 0.447(1)]$ in [26] using predictions about scaling of entanglement entropy for a CFT. There it was also shown that the entanglement entropy and the kinetic term in the Hamiltonian could be used to illustrate the phase diagram, as we have done here with the fluctuation of the electric field and the on-site occupation of the bosons.

The analysis of Ref. [26] using the well-established machinery of CFT predicted the existence of a direct sum of two critical theories—free Majorana fermion and free boson—at the critical point. In this work, we complement the previous work with a proper characterization of these two gapless modes.

C. Sound velocity at criticality

To verify that the critical point $(\mu_c^2/q^2 = 0.447, \lambda_c/q^2 = 0.0565)$ displays Lorentz invariance in its low-energy description, we calculate the sound velocity v_s at the critical point from the scaling of ground-state energy—recapitulating the result presented in the supplemental material of Ref. [26]. For a Lorentz invariant system exhibiting a linear dispersion at low energies, the ground-state energy E_0 , under open boundary conditions, scales with the system size L according to [60–62]

$$E_0(L) = \epsilon_0^\infty L + \epsilon_1^\infty - \frac{\pi c v_s}{24L}, \quad (7)$$

where ϵ_0^∞ is the ground-state energy density in the bulk, ϵ_1^∞ is the surface free energy in the thermodynamic limit, c is the central charge of the corresponding CFT, and v_s is the sound velocity. It should be noted that v_s vanishes for Lorentz noninvariant critical points characterized by a quadratic dispersion.

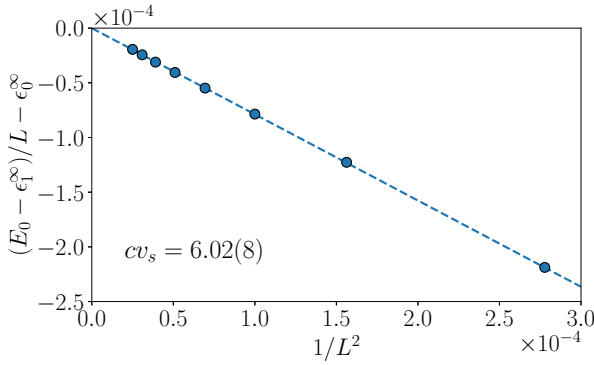


FIG. 3. Finite-size scaling of the ground-state energy E_0 at the critical point according to Eq. (7), which gives $cv_s \simeq 6$, where c is the central charge and v_s is the sound velocity.

To estimate v_s , we perform the finite-size scaling of the ground-state energy according to Eq. (7) at the critical point (for a similar scaling analysis, see [63–66]). The finite-size scaling (Fig. 3) reveals

$$cv_s = 6.02 \pm 0.08, \quad (8)$$

confirming the Lorentz invariance of the critical point ($\mu_c^2/q^2 = 0.447$, $\lambda_c/q^2 = 0.0565$) and the applicability of the CFT framework.

III. NUMERICAL RESULTS

Here we describe our numerical results that contribute to clarifying the nature of the field theory emerging at the critical point of the lattice model. For this, we set $\lambda/q^2 = 0.0565$ and $\mu^2/q^2 = 0.447$ in the rest of the paper.

To reiterate, we employ DMRG simulations to extract the low-lying spectrum of the Hamiltonian (6) with $U(1)$ symmetric MPS [67,68]. The MPS bond dimension used in our study is up to $\chi = 600$, sufficient for convergence up to system sizes 120. Each of the bosonic species, a and b , has been truncated to 11 levels, leading to the physical dimension of 121 for the MPS tensors. Furthermore, in Sec. III B 1, we also simulate the full matter-gauge Hamiltonian (2). In that case, the MPS ansatz contains alternating tensors for matter and gauge degrees of freedom (see Fig. 1). The gauge fields are then truncated to up to 15 levels in the electric basis. Details about the MPS-based numerical calculations are presented in Appendix A.

For the out-of-equilibrium analysis presented in Sec. III D, we use TDVP algorithms as described in [37]. To reduce the computational complexity of TDVP runs, we truncate the bosonic species up to eight levels, and the maximum MPS bond dimension is restricted up to $\chi = 400$.

A. The scaling of Renyi entanglement entropy

The Renyi entanglement entropy of order n for a block of l sites is defined as

$$S_n(l) = \frac{1}{1-n} \log(\text{Tr} \rho_l^n), \quad (9)$$

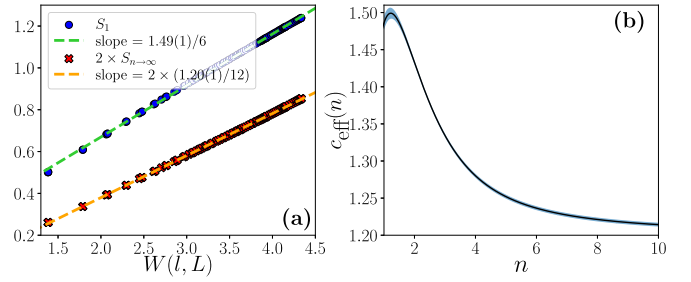


FIG. 4. (a) The variation of the von Neumann entanglement entropy $S = S_{n \rightarrow 1}$ and the entanglement ground-state energy $\varepsilon = S_{n \rightarrow \infty}$ as a function of the chord length W according to Eq. (10) at the critical SOQPT point. (b) The extracted values of the central charge after fitting the Renyi entropy data to Eq. (10). The bluish shade describes the error-bars in fitted values of $c_{\text{eff}}(n)$. For these plots, we have analyzed the data for system-sizes $L \in [40, 60, 80, 100, 120]$ at the critical point ($\lambda_c/q^2 = 0.0565$, $\mu_c^2/q^2 = 0.447$).

where $\rho_l = \text{Tr}_{l+1, l+2, \dots, L} |\psi\rangle\langle\psi|$ is the reduced density matrix after tracing out the rest of the system. As limiting cases of the Renyi entropy, we get the von Neumann entropy as $S = \lim_{n \rightarrow 1} S_n$ and the entanglement ground-state energy $\varepsilon_0 = \lim_{n \rightarrow \infty} S_n$, where ε_0 is the lowest eigenvalue of the entanglement Hamiltonian $H_l = -\log(\rho_l)$, i.e., $\varepsilon_0 = -\log \lambda_0$, where λ_0 is the smallest eigenvalue of the density matrix ρ_l . It should be noted that since we are integrating out the gauge fields, the resulting Hilbert space of matter has a well-defined tensor-product structure and there are no ambiguities in defining the bipartitions associated with the gauge invariance (cf., [69–71]).

In a CFT, the finite-size scaling of the Renyi entanglement entropy of the bipartition of size l in a chain with open boundary conditions and length L is [72–74]

$$S_n(l, L) = \frac{c}{12} \left(1 + \frac{1}{n} \right) W + b'_n, \quad (10)$$

where c is the central charge of the corresponding CFT, b'_n is a nonuniversal constant, and W , the chord length, is a function of both L and l :

$$W(l, L) = \log \left[\frac{2L}{\pi} \sin(\pi l/L) \right]. \quad (11)$$

In Ref. [26], using the above scaling of von Neumann entropy at the critical point, a central charge of $c = 3/2$ [$c = 1.49(1)$ to be precise] has been extracted [see Fig. 4(a)]. It has been argued in [26] that this value of the central charge can be explained as the sum of two different minimal models, each contributing to a piece of the total central charge, a $c_f = 1/2$ for a free Majorana fermion (the Ising sector) and a $c_b = 1$ for a free boson.

However, performing the same scaling for the entanglement ground-state energy ε_0 , the effective central charge comes out to be $c_{\text{eff}}(n \rightarrow \infty) = 1.20(1)$ [see Fig. 4(a)], which contradicts the value $c = 3/2$. Moreover, upon closer inspection, we find that the values of central charge obtained by fitting the entropy data to Eq. (10) are heavily dependent on the order n as seen in Fig. 4(b).

Nevertheless, the analyses in Sec. II C and in the following Sec. III D suggest that the central charge of the system is

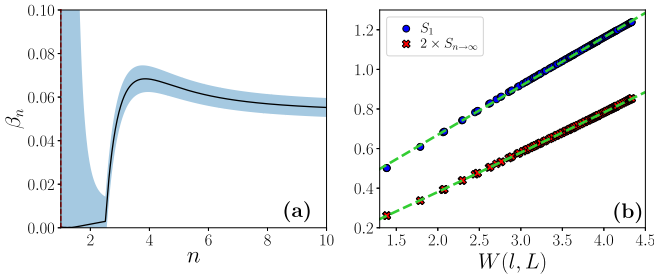


FIG. 5. (a) The exponent β_n in the finite-size correction to the entanglement entropy scaling [see Eq. (12)] as a function of the Renyi order n . Here we fix $c = 3/2$ (see the text). The bluish shade describes the error bars in fitted values of β_n . Note that the error in the fitting is large when $c_{\text{eff}} \sim 3/2$ as the curve-fitting becomes ill-formed with redundant parameters within that regime. (b) The fitting of von Neumann entanglement entropy $S = S_1$ and the entanglement ground-state energy $\varepsilon = S_{n \rightarrow \infty}$ including the correction term as in Eq. (12). Note that the entropic data (symbols) are exactly the same as in Fig. 4(b)—the difference lies in the use of Eq. (12) in fitting these data. All other descriptions are the same as those in Fig. 4.

indeed compatible with $c = 3/2$. In Sec. II C, by utilizing the finite-size scaling of ground-state energy, we have shown that $cv_s \simeq 6$, whereas using the out-of-equilibrium local quench spectroscopy in the following Sec. III D we verify that the sound velocity is consistent with $v_s = 4$, thereby leaving $c = 3/2$ as the only possibility. These results are obviously independent of the entropy scaling.

Here, we try to explain the discrepancies in the scaling of different Renyi entropies by finite-size corrections in the scaling law of Eq. (10). Specifically, it has been shown in [75] that due to irrelevant and marginally irrelevant bulk operators in the Hamiltonian, the Renyi entropies can attain corrections in finite systems, where the correction terms can depend on n and on the scaling dimensions of such bulk operators (see also [76,77]). Since the numerical determination of the scaling dimensions of such irrelevant (or marginally irrelevant) bulk operators can be very nontrivial, here we consider a generic correction term, having the same form as in [75], to the scaling formula of Eq. (10) as follows:

$$S_n(l, L) = \frac{c}{12} \left(1 + \frac{1}{n} \right) W + b'_n + d_n [\exp(W)]^{-\beta_n}, \quad (12)$$

where d_n and β_n are n -dependent quantities to be determined. It should be noted that since Eq. (12) has four independent parameters, the curve-fitting process is under constraint for the given entropic data, leading to unfaithful extraction of these parameters. Because of this, we fix the central charge to $c = 3/2$, verified independently from the ground-state energy scaling in Sec. II C [see Eq. (8)] and the local quench spectroscopy in Sec. III D, when fitting Eq. (12) to the entropic data.

The variation of the exponent β_n as a function of the order n is shown in Fig. 5(a) along with its errors for fixed $c = 3/2$. For small n , corrections to the original formula are small (the corresponding error is not informative as such a term does not contribute to the fit). Oppositely, for large n , where we observe $c_{\text{eff}} \approx 3/2$ [Fig. 4(b)], corrections are indeed strong and the coefficient β_n is essentially n -independent. This strongly

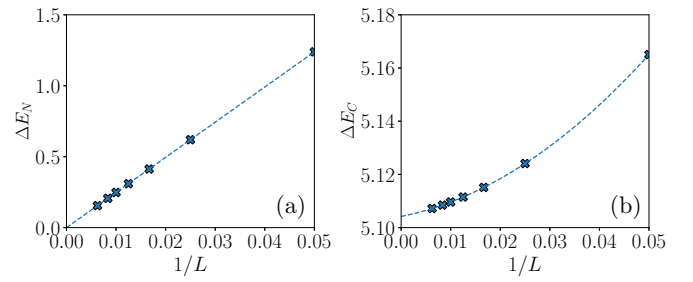


FIG. 6. The scalings of (a) the neutral gap ΔE_N and (b) the charge gap ΔE_C with the system-size L at the critical SOQPT point. The neutral gap decays to zero in the thermodynamic limit as $\sim 1/L$, while the charge gap remains finite and its thermodynamic value [5.104(4)] is extracted by fitting a quadratic function in $1/L$.

confirms the fact that extracting the central charge from such large- n Renyi entropies is not reliable using the original scaling relation when finite-size effects are strong. Figure 5(b) shows the actual entropy scalings for the von Neumann entanglement entropy $S = S_1$ and the entanglement ground-state energy $\varepsilon = S_{n \rightarrow \infty}$ according to Eq. (12) with fixed $c = 3/2$.

B. Spectral analysis at equilibrium

To detect and characterize the Majorana fermionic and the bosonic part of the theory, we first analyze the energies of the ground state and low-lying excited states and their finite-size scaling at the critical point ($\lambda_c/q^2 = 0.0565$, $\mu_c^2/q^2 = 0.447$) obtained from DMRG simulations.

1. The neutral gap and the charge gap

We calculate the neutral gap (ΔE_N) and the charge gap (ΔE_C) at the critical point. The gaps are defined as

$$\begin{aligned} \Delta E_N &= E_1(Q=0) - E_0(Q=0), \\ \Delta E_C &= E_0(Q=1) + E_0(Q=-1) - 2E_0(Q=0), \end{aligned} \quad (13)$$

where $E_n(Q)$ represents the n th energy eigenvalue at the $Q = \langle \hat{Q} \rangle$ quantum sector extracted by means of the excited-state DMRG.

As expected, the neutral gap ΔE_N decays to zero in the thermodynamic limit as $\sim 1/L$ [see Fig. 6(a)]. On the other hand, quite interestingly, the charge gap ΔE_C saturates to a finite value $\Delta E_C = 5.104(4)$ in the thermodynamic limit [see Fig. 6(b)]. This happens due to the gauge invariance of the system, as a single charge excitation must be accompanied by a string of electric fields (semi-infinite in the thermodynamic limit) whose energy cannot vanish.

Therefore, by imposing the Gauss law, we are throwing away a large chunk of the low-energy spectrum. This is illustrated in Fig. 7, where we show that there are indeed many low-lying states that come from other gauge sectors (i.e., nonzero background fields) by performing the excited-state DMRG calculations for the matter-gauge Hamiltonian (2). It should be noted that since gauge invariance cannot be broken spontaneously, the excited-state DMRG cannot scan all possible low-lying gauge sectors, and its reliability in iteratively finding excited states one after another degrades very quickly when we do not impose the Gauss law.

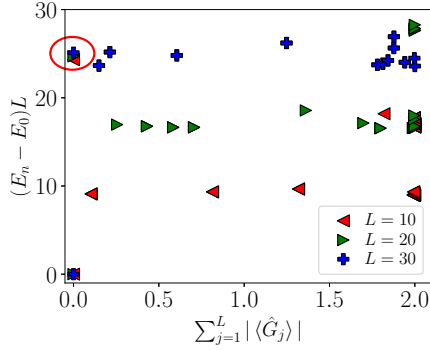


FIG. 7. Energy gaps of a few excited states obtained from the excited-state DMRG when we do not enforce the Gauss law by integrating out the gauge fields, and instead treat the Hamiltonian (2) as it is with conserved total charge $Q = 0$. Here, we truncate the gauge fields to 15 electric levels. The x -axis, $\sum_{j=1}^L |\langle \hat{G}_j \rangle|$, denotes the deviation from the Gauss law $\langle \hat{G}_j \rangle = 0$ for all $j = 1, \dots, L$. The red circle demarcates the first neutral excitations that obey the Gauss law. Note here that the excited-state DMRG is unable to find all the low-lying states coming from different gauge sectors, specifically when $\sum_{j=1}^L |\langle \hat{G}_j \rangle| \neq 0$. Nevertheless, we can see the existence of many low-lying states coming from different gauge sectors in the low-energy spectrum.

2. Conformal towers

Here, we analyze the excitation spectra of the system at a critical point using the predictions of CFT by using the excited-state DMRG. The excited-state energies vary with the system-size as

$$E_n(L) = E_0(L) + x_n \frac{\pi v_s}{L}, \quad (14)$$

where x_n are boundary scaling dimensions, organized in conformal towers [78,79]. In Fig. 8, we plot $x_n = (E_n - E_0)L/\pi v_s$ for the first nine excited states along with their degeneracies obtained from the excited-state DMRG calculations. The boundary exponents that we get from Fig. 8 are $x_n = [2, 3, 4, 5, 6, \dots]$ with degeneracies $[1, 1, 2, 2, 3, \dots]$. These values of the boundary exponents and corresponding degeneracies match with the CFT prediction for the critical

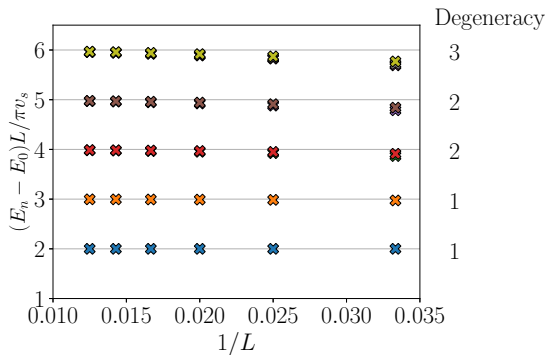


FIG. 8. First few boundary scaling dimensions $x_n = (E_n - E_0)L/\pi v_s$ in the conformal tower of the critical point using the excited-state DMRG.

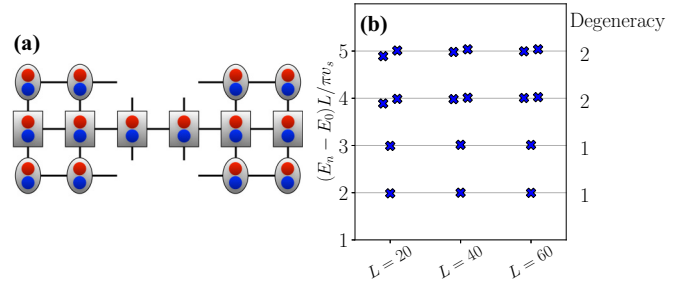


FIG. 9. (a) The graphical representation of the midchain effective Hamiltonian constructed from the MPO and MPS tensors to target the ground state of the Hamiltonian (6). (b) The excitation spectra of the effective Hamiltonian depicted in (a) at the critical point.

Ising model with a fixed boundary condition [66,80,81]. This structure of the conformal tower confirms the Ising or free Majorana fermion part of the critical point. On the other hand, we completely miss the bosonic part of the spectrum at the critical point. However, we can make an educated guess based on the results of Sec. III B 1 (specifically, of Fig. 7) that the bosonic excitations, which carry charges, might be hidden in other gauge sectors.

To validate this result further, we analyze the spectra of the effective Hamiltonian constructed to target the ground states of the Hamiltonian (6) during DMRG sweeps [see Fig. 9(a)]. In Ref. [66], it has been shown that at the critical point, the low-lying eigenstates of the effective Hamiltonian, within the framework of the standard ground-state algorithm, give correct excitation spectra of the original Hamiltonian. In Fig. 9(b) we show the first few eigenstates of the effective Hamiltonian at the critical point. Once again, the extracted boundary exponents and corresponding degeneracies match with the Ising CFT.

C. Determination of the Luttinger parameter

Since we could not characterize the bosonic part of the critical theory from the low-energy excitation spectrum, we take the route of determining the Luttinger parameter K associated with the free bosonic part that is described by the Tomonaga-Luttinger liquid theory [82,83]. Here, we extract K from the scaling of the bipartite fluctuations as described in Refs. [84–86], under the assumption that charge excitations are indeed those responsible for the emergence of the $c_b = 1$ sector of theory. It has been shown that in a Tomonaga-Luttinger liquid, for a global $U(1)$ conserved quantity O , the local fluctuations

$$\mathcal{F}_l(O) = \left\langle \left(\sum_{j \leq l} O_j \right)^2 \right\rangle - \left\langle \sum_{j \leq l} O_j \right\rangle^2 \quad (15)$$

obey the scaling of the form

$$\mathcal{F}_l(O) = \frac{K}{2\pi^2} W(l, L) + \text{const.} \quad (16)$$

In the present scenario, the global conserved quantity is the total dynamical charge \hat{Q} . Using the local gauge invariance, we can also rewrite the local fluctuations of the dynamical

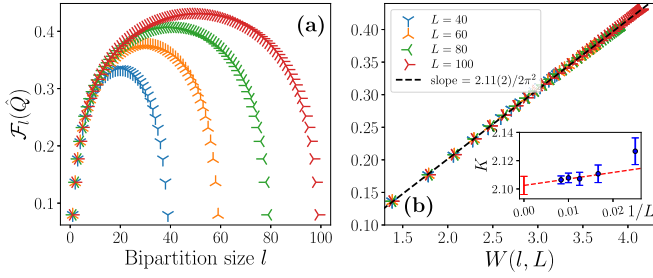


FIG. 10. The scaling of local fluctuations $\mathcal{F}_l(\hat{Q})$ in relation to the chord length $W(l, L)$. (a) The pattern of local fluctuations with respect to the bipartition size for different system sizes is plotted and indicated in the figure. (b) The fit performed with the data for $L \in [40, 60, 80, 100, 120]$, based on Eq. (16), suggests that the Luttinger parameter is $K = 2.11(2)$. The inset shows the negligible dependence of K on the system size. To estimate the Luttinger parameter K at the thermodynamic limit, we extrapolate the extracted values of K for different system-sizes $L \in [60, 120]$ using a linear fit in $1/L$, yielding $K = 2.10(1)$.

charge as

$$\mathcal{F}_l(\hat{Q}) = \langle \hat{L}_l^2 \rangle - \langle \hat{L}_l \rangle^2, \quad (17)$$

where we have used the fact that $\hat{L}_l = \sum_{j \leq l} \hat{Q}_j$. In Fig. 10, we present the variations of local fluctuations as a function of both bipartition and system size. This figure provides evidence that the Luttinger parameter is $K = 2.10(1)$, which characterizes the existence of a strongly interacting bosonic component in the theory.

D. Spectral analysis from out-of-equilibrium dynamics

We now analyze the critical point by considering the response of the system to a local quench as suggested in [87,88]. For that, we create a local excitation at the middle of the chain using the operator

$$\hat{\mathcal{M}}^Q = \hat{\phi}_{L/2}^\dagger \hat{\phi}_{L/2+1} \quad (18)$$

that will create $Q = \pm 1$ dynamical charges at sites $L/2$ and $L/2 + 1$, respectively, on top of the ground state $|\Omega\rangle$, such that our initial state becomes

$$|\psi^Q\rangle(t=0) = \mathcal{N} \hat{\mathcal{M}}^Q |\Omega\rangle, \quad (19)$$

where \mathcal{N} is a normalization constant. Since the operator $\hat{\mathcal{M}}^Q$ is a local element of the Hamiltonian (6), we can expect that the overlaps of $|\psi^Q\rangle$ with low-lying excited states are nonvanishing.

For any local observable \hat{O}_j , we analyze the spectral properties by means of the (discrete) Fourier transform:

$$\mathcal{F}_O(k, \omega) = \frac{2\pi}{LT} \delta t \sum_{j=1}^L e^{-ik(j-\frac{L}{2})} \sum_{n=0}^{t_N} e^{-i\omega t_n} (\langle O_j \rangle(t_n) - \langle O_j \rangle_\Omega), \quad (20)$$

where $t_n = n\delta t$ is the discrete time-steps, $T = t_N \delta t$ is the total time of the evolution, and $\langle O_j \rangle_\Omega$ defines the expectation value of \hat{O}_j with respect to the ground state $|\Omega\rangle$ (see [59] for details).

Since the neutral gap vanishes while the charge gap remains finite at the critical point, we expect that for neutral operators such as $\hat{\phi}_j^\dagger \hat{\phi}_j$, $\hat{\Pi}_j^\dagger \hat{\Pi}_j$, or $\hat{L}_j = (\sum_{l \leq j} \hat{Q}_l)^2$

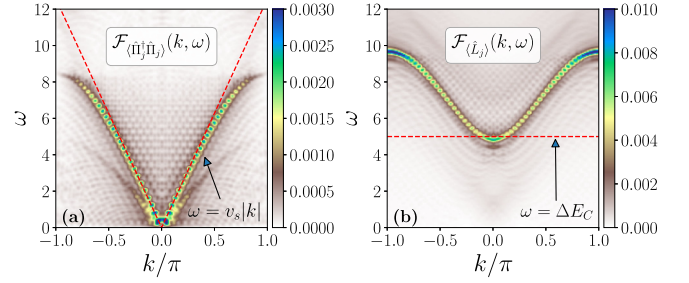


FIG. 11. The dispersion relations from the Fourier transform [Eq. (20)] of the local operators (a) $\hat{\Pi}_j^\dagger \hat{\Pi}_j$ and (b) \hat{L}_j at the critical point for the initial state (19) for a system of size $L = 60$. Here we apply the operator $\hat{\mathcal{M}}^Q$ [see Eq. (18)] to excite the ground state.

the Fourier transform will provide a gapless dispersion with $\omega(k) \approx v_s |k|$ for $k \ll 1$, and for any charge carrying operators like \hat{Q}_j or $\hat{L}_j = \sum_{l \leq j} \hat{Q}_l$, the $\mathcal{F}_O(k, \omega)$ will give a gapped spectrum [87,88].

From the Fourier transform of the neutral operators, e.g., $\mathcal{F}_{(\hat{\Pi}_j^\dagger \hat{\Pi}_j)}(k, \omega)$ in Fig. 11(a), we are getting the gapless spectrum as expected. The signal in the Fourier transform matches with $v_s \approx 4$ [red dashed line in Fig. 11(a)] extracted from the scaling of ground-state energy (see Sec. II C). Upon careful inspection, we find another faint signal corresponding to $v_s \approx 2.4$. However, this value of the sound velocity is not consistent with earlier equilibrium analysis coming from the scaling of ground-state energy [Eq. (8)]. This faint signal might be a spurious effect coming from numerical errors, as also seen in [59]. There is also a possibility that this might come from the dispersion in $Q = \pm 1$ sectors as the excitation performed by the operator $\hat{\mathcal{M}}^Q$ couples these sectors to the present $Q = 0$ one. On the other hand, in Fig. 11(b), we see that the dispersion relation from $\mathcal{F}_{(\hat{L}_j)}(k, \omega)$ is gapped and the gap is exactly the same as the charge gap ΔE_C .

To be sure that there is only one sound velocity at $v_s = 4$, we perform two other forms of time-evolution in such a way that the local excitation now does not create any dynamical charges so that we can solely examine the neutral excitations. Specifically, we excite the ground state $|\Omega\rangle$ with the neutral operators

$$\hat{\mathcal{M}}^1 = \hat{\phi}_{L/2}^\dagger \hat{\phi}_{L/2} \hat{\phi}_{L/2+1}^\dagger \hat{\phi}_{L/2+1}, \quad (21)$$

$$\hat{\mathcal{M}}^2 = \hat{\phi}_{L/2}^\dagger \hat{\phi}_{L/2} + \hat{\phi}_{L/2+1}^\dagger \hat{\phi}_{L/2+1}, \quad (22)$$

and then perform a similar Fourier analysis as before.

In Fig. 12, we show the Fourier transforms of $\hat{\Pi}_j^\dagger \hat{\Pi}_j$ for such initial states. Clearly, there is only one sound velocity of $v_s = 4$ that we can observe.

IV. CONCLUSIONS

In this article, we presented an in-depth analysis of the critical properties of the 1+1D Abelian-Higgs model on a discretized lattice. Our approach provides a comprehensive understanding of the model's behavior, including its bosonic and fermionic components.

First, we addressed the ambiguity surrounding the value of the central charge at the critical point. We confirmed that the central charge is $c = 3/2$, which can be interpreted as

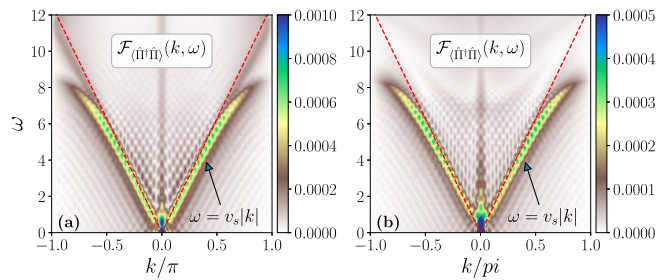


FIG. 12. Same as in Fig. 11(a) but for the initial states excited with the operators given in (a) Eq. (21) and (b) Eq. (22).

a direct sum of gapless compactified bosons with $c_b = 1$ and critical Majorana fermions with $c_f = 1/2$. We independently corroborated this value from both equilibrium and out-of-equilibrium analysis. Our results also reveal that the discrepancy in extracting the central charge from different Renyi entropies can be attributed to finite-size effects coming from irrelevant or marginally irrelevant bulk operators.

To identify the bosonic and fermionic components of the model, we have used a twofold approach. First, we find that the excitation spectrum of the model is identical to that of the critical Ising chain with fixed boundary conditions, i.e., the $c = 1/2$ free fermionic part. Quite interestingly, we find no sign of the bosonic excitations in the gauge-invariant spectrum. Our examination of the excitation spectrum in different superselection sectors leads us to make an informed guess that the bosonic excitation spectrum may be “hidden” in other gauge sectors. We have then determined the Luttinger parameter, which confirms the existence of a gapless Tomonaga-Luttinger liquid with a value of Luttinger parameter $K \approx 2.1$.

The fact that the bosonic spectrum that contributes to the entanglement entropy at the critical point could be hidden in different superselection sectors suggests that a better understanding of the boundary CFT involved with the computation of the entanglement entropy here could be necessary. Also, some further hints could be obtained from the analysis of the symmetry-resolved entanglement spectrum that will be performed elsewhere.

Finally, we analyzed the local quenched dynamics of the critical system. By performing spectroscopy via discrete Fourier transform, we extract the dispersion relations for the interacting system. Our analysis reveals that there exists only one speed of sound in this gauge-invariant system, which is consistent with our equilibrium analysis.

ACKNOWLEDGMENTS

We acknowledge the PL-GRID infrastructure for providing us with the high-performance computing facility under Grant No. PLG/2022/015613, which yielded the numerical results reported here. The MPS algorithms have been implemented using ITensor library [89,90]. The work of M.D. was partly supported by the ERC under Grant No. 758329 (AGEnTh), the MIUR Programme FARE (MEPH), the QUANTERA DYNAMITE PCI2022-132919, and the European Union’s Horizon 2020 research and innovation programme under Grant Agreement No. 817482

(Pasquans). M.L. acknowledges support from: ERC AdG NOQIA; MCIN/AEI (PGC2018-0910.13039/501100011033, CEX2019-000910-S/10.13039/501100011033, Plan National FIDEUA PID2019-106901GB-I00, Plan National STAMEENA PID2022-139099NB-I00 project funded by MCIN/AEI/10.13039/501100011033 and by the “European Union NextGenerationEU/PRTR” (PRTR-C17.I1), FPI); QUANTERA MAQS PCI2019-111828-2); QUANTERA DYNAMITE PCI2022-132919 (QuantERA II Programme co-funded by European Union’s Horizon 2020 program under Grant Agreement No. 101017733), Ministry of Economic Affairs and Digital Transformation of the Spanish Government through the QUANTUM ENIA project call – Quantum Spain project, and by the European Union through the Recovery, Transformation, and Resilience Plan – NextGenerationEU within the framework of the Digital Spain 2026 Agenda; Fundació Cellex; Fundació Mir-Puig; Generalitat de Catalunya (European Social Fund FEDER and CERCA program, AGAUR Grant No. 2021 SGR 01452, QuantumCATV16-011424, co-funded by ERDF Operational Program of Catalonia 2014-2020); Barcelona Supercomputing Center MareNostrum (FI-2023-1-0013); EU Quantum Flagship (PASQuanS2.1, 101113690); EU Horizon 2020 FET-OPEN OPTologic (Grant No. 899794); EU Horizon Europe Program (Grant Agreement No. 101080086 – NeQST), ICFO Internal “QuantumGaudi” project; European Union’s Horizon 2020 program under the Marie Skłodowska-Curie Grant Agreement No. 847648; “La Caixa” Junior Leaders fellowships, “La Caixa” Foundation (ID 100010434): CF/BQ/PR23/11980043. This research was also funded by National Science Centre (Poland) by Grant No. 2021/03/Y/ST2/00186 within the QuantEra II Programme, which has received funding from the European Union’s Horizon 2020 research and innovation programme under Grant Agreement No. 101017733 DYNAMITE (J.Z.). The partial support by the Strategic Programme Excellence Initiative at Jagiellonian University is also acknowledged. L.T. acknowledges the support from the Spanish project PGC2018-095862-B-C22, the CSIC Interdisciplinary Thematic Platform (PTI) Quantum Technologies (PTI-QTEP+), and from the Spanish projects PID2021-127968NB-I00 and TED2021-130552B-C22 funded by MCIN/AEI/10.13039/501100011033/FEDER, UE and MCIN/AEI/10.13039/501100011033, respectively.

Views and opinions expressed in this work are, however, those of the authors only and do not necessarily reflect those of the European Union, European Climate, Infrastructure and Environment Executive Agency (CINEA), nor any other granting authority. Neither the European Union nor any granting authority can be held responsible for them.

APPENDIX A: DETAILS ABOUT THE MATRIX PRODUCT STATES SIMULATIONS

In this paper, we use matrix product states (MPSs) [38,39] based tensor network simulations to obtain the results. Specifically, to extract the ground state and low-lying excited states, we use a strictly single-site variant of the density matrix renormalization group (DMRG) algorithm [52–55] with subspace expansion [91]. For the out-of-equilibrium real-time

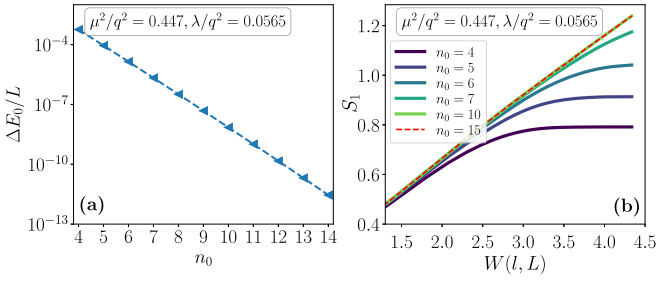


FIG. 13. (a) The convergence of ground-state energy density with respect to the maximum bosonic occupancy n_0 for a system of size $L = 120$ at the critical point. Here we plot the relative errors in the energy density $\Delta E_0/L$, where $\Delta E_0 = |E_0(n_0) - E_0(n_0 + 1)|$. (b) The profile of the von Neumann entanglement entropy $S = S_1$ with respect to the cord length $W = \ln(\frac{2L}{\pi} \sin(\pi l/L))$ at the critical point for $L \in [40, 120]$ and for different values of n_0 .

dynamics, we employ the time-dependent variational principle (TDVP) method [56–59].

In our MPS representation, we truncate the Hilbert spaces of both the bosonic species, a and b , up to the maximum occupancy of $n_0 = 10$ (i.e., 11 levels of each type of bosonic matter), which results in the physical dimension of 121 for the MPS tensors on the matter sites. To verify the convergence with respect to this cutoff, we vary the maximum bosonic occupancy n_0 in the range [4, 15], and we check for convergence of different observables (see Fig. 13). Specifically, we show in Fig. 13(a) that for $n_0 = 10$ the error in the ground-state energy density for system-size $L = 120$ falls below 10^{-7} at the critical point. Moreover, the entropy profile for $n_0 = 10$ is essentially identical to the one with $n_0 = 15$, capturing the proper entropy scaling with respect to the cord length [Fig. 13(b)]. For the simulating short-range matter-gauge Hamiltonian (2), we truncate the gauge field Hilbert spaces to 15 levels in electric basis (see Appendix B).

For the DMRG simulations, the MPS bond dimension is truncated up to $\chi = 600$. Figure 14(a) shows the convergence

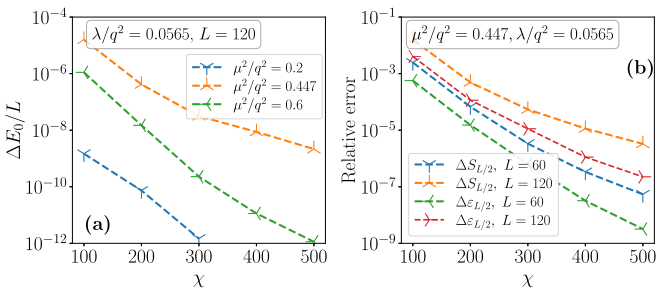


FIG. 14. The convergence of (a) the energy density ($\Delta E_0/L$) and (b) the half-chain von Neumann entanglement entropy ($\Delta S_{L/2}$) and the half-chain entanglement ground-state energy ($\Delta \varepsilon_{L/2}$) with respect to the maximum bond dimension used in the simulation, respectively, $\chi \in \{100, 200, 300, 400, 500, 600\}$. Here we plot relative errors in the quantities as $\Delta O = |O_\chi - O_{\chi+100}|$. In (a) we choose three points in the phase diagram, namely (1) a point in the confined phase ($\mu^2/q^2 = 0.2$), (2) the critical point ($\mu^2/q^2 = 0.447$), and (3) a point in the Higgs phase ($\mu^2/q^2 = 0.6$) for the system-size $L = 120$. In (b) we show the convergence of the entropic quantities as a function of the bond dimension at the critical point.

of the ground-state energy density with respect to the bond dimension $\chi \leq 600$ for systems of sizes $L \leq 120$. The energy density converges close to machine precision within $\chi \leq 500$ in the gapped regions—confined ($\mu^2/q^2 = 0.2$) and Higgs (μ^2/q^2). On the other hand, as expected, the convergence is slower at the critical point due to the diverging correlation length. However, as shown in Fig. 14(b), the precision attained

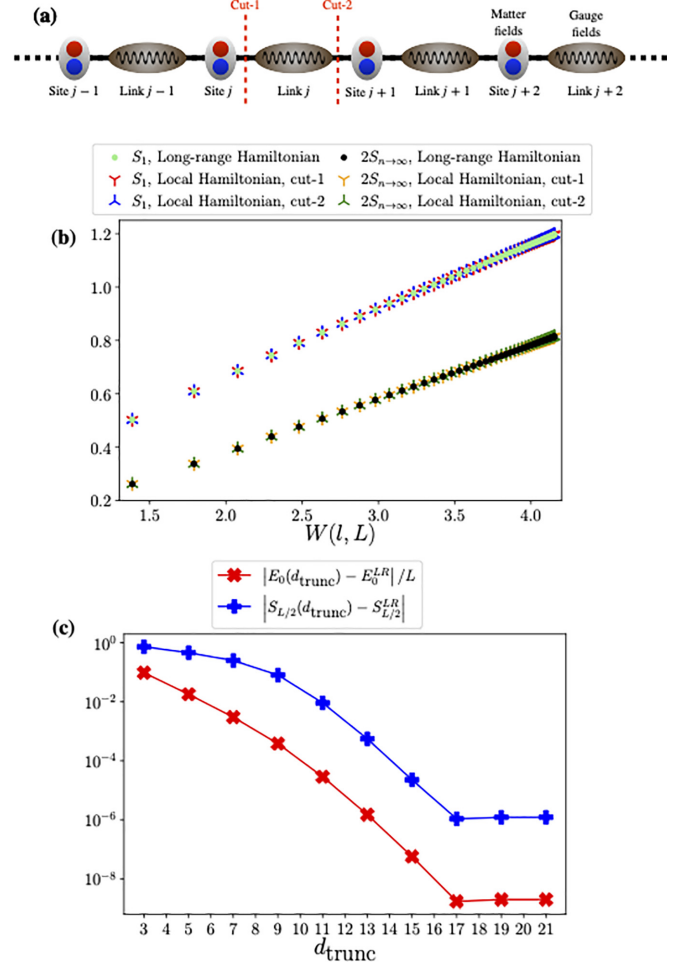


FIG. 15. (a) In the presence of gauge fields at the links between two nearest-neighbor sites, there are two options to take bipartition at a given link, i.e., cut-1 and cut-2 depicted in the figure, for the calculation of entanglement entropies. The entropies, however, remain the same between these two options since gauge fields in 1+1D are not dynamical variables. (b) The comparison between von Neumann entropy $S = S_1$ and the entanglement ground-state energy $\varepsilon_0 = S_{n \rightarrow \infty}$ calculated from the long-range Hamiltonian after integrating-out the gauge fields and from the original local matter-gauge Hamiltonian for system-size $L = 100$ at the critical point. For the local gauge theory Hamiltonian, we truncate the gauge-field Hilbert spaces up to $d_{\text{trunc}} = 21$ electric states. (c) We plot the absolute differences in ground-state energy densities and in the midchain von Neumann entanglement entropies between the truncated local matter-gauge Hamiltonian with respect to the long-range system as a function of the truncated gauge-field Hilbert-space dimension d_{trunc} . Here we consider the system size $L = 60$. The differences reduce to the numerical accuracy attained with the MPS bond dimension $\chi = 600$ at the truncation level $d_{\text{trunc}} = 17$.

at the critical point for $\chi = 500, 600$ is sufficient to perform the precise scaling analysis reported here. To confirm the convergence of the DMRG sweeps, we continue the DMRG iterations until the energy difference in subsequent sweeps falls below 10^{-13} .

In the case of out-of-equilibrium simulations with TDVP, we truncate the bosonic species up to the maximum occupancy of $n_0 = 7$ (i.e., eight levels), and we restrict the maximum MPS bond up to $\chi = 400$.

APPENDIX B: NUMERICAL COMPARISONS BETWEEN THE LOCAL MATTER-GAUGE AND THE MATTER-ONLY LONG-RANGE DESCRIPTIONS OF THE SYSTEM

In the main text, we have favored the long-range Hamiltonian (6) after integrating-out the gauge fields by an exact mapping utilizing the Gauss law. This is because of the advantage in the long-range formulation, where we avoid dealing with extra degrees of freedom corresponding to the gauge fields. Moreover, since the Hilbert spaces of the gauge fields are formally infinite-dimensional, they need to be truncated to a finite-dimensional subspace in the short-range formulation of Eq. (2), thereby introducing an extra source of approximation that needs to be accurately controlled (see, e.g., [42]).

Here, we show that the short-range Hamiltonian, with sufficiently large truncated gauge-field Hilbert spaces, gives the exact same results as that of the long-range Hamiltonian discussed in the main text.

In the presence of the gauge fields in the short-range formulation, we have two options to take bipartitions at each link—one before the gauge field (cut-1) and another after the gauge field (cut-2)—for the calculation of entanglement entropies as seen in Fig. 15(a). In Figs. 15(b) and 15(c), we compare the results between the truncated short-range matter-gauge Hamiltonian (2) and the long-range Hamiltonian (6). First, we can observe that in the case of local gauge theory, entropies calculated at cut-1 or cut-2 are the same, which is expected since the gauge fields are not dynamical variables in 1+1D; see Fig. 15(b). Moreover, with sufficiently large gauge-field Hilbert space dimension (d_{trunc}), local and long-range Hamiltonians give exactly the same result [up to a numerical accuracy; see Fig. 15(c)]. This is understandable as in 1+1D, integrating-out the gauge fields using the Gauss law is exact. Specifically, Fig. 15(c) shows that the differences between the results coming from the truncated local gauge theory Hamiltonian and those from the long-range Hamiltonian reduce to the numerical accuracy (attained with the MPS bond dimension $\chi = 600$) for $d_{\text{trunc}} \geq 17$.

-
- [1] S. Coleman, *Aspects of Symmetry* (Cambridge University Press, Cambridge, 1985).
- [2] P. D. Francesco, P. Mathieu, and D. Sénéchal, *Conformal Field Theory* (Springer, New York, 1997).
- [3] R. Blumenhagen and E. Plauschinn, *Introduction to Conformal Field Theory* (Springer, Berlin, 2009).
- [4] R. Shankar, *Quantum Field Theory and Condensed Matter* (Cambridge University Press, Cambridge, 2017).
- [5] E. Fradkin, *Field Theories of Condensed Matter Physics* (Cambridge University Press, Cambridge, 2013).
- [6] K. G. Wilson, *Phys. Rev. B* **4**, 3174 (1971).
- [7] K. G. Wilson, *Phys. Rev. B* **4**, 3184 (1971).
- [8] K. G. Wilson, *Rev. Mod. Phys.* **47**, 773 (1975).
- [9] R. Shankar, *Rev. Mod. Phys.* **66**, 129 (1994).
- [10] M. Gell-Mann and F. E. Low, *Phys. Rev.* **95**, 1300 (1954).
- [11] M. E. Peskin and D. V. Schroeder, *An Introduction to Quantum Field Theory* (Addison-Wesley, Reading, MA, 1995).
- [12] M. D. Schwartz, *Quantum Field Theory and the Standard Model* (Cambridge University Press, Cambridge, 2013).
- [13] P. W. Anderson, *Phys. Rev.* **130**, 439 (1963).
- [14] F. Englert and R. Brout, *Phys. Rev. Lett.* **13**, 321 (1964).
- [15] P. W. Higgs, *Phys. Rev. Lett.* **13**, 508 (1964).
- [16] G. S. Guralnik, C. R. Hagen, and T. W. B. Kibble, *Phys. Rev. Lett.* **13**, 585 (1964).
- [17] M. Endres, T. Fukuhara, D. Pekker, M. Cheneau, P. Schauß, C. Gross, E. Demler, S. Kuhr, and I. Bloch, *Nature (London)* **487**, 454 (2012).
- [18] K. Kasamatsu, I. Ichinose, and T. Matsui, *Phys. Rev. Lett.* **111**, 115303 (2013).
- [19] D. Pekker and C. Varma, *Annu. Rev. Condens. Matter Phys.* **6**, 269 (2015).
- [20] Y. Kuno, S. Sakane, K. Kasamatsu, I. Ichinose, and T. Matsui, *Phys. Rev. D* **95**, 094507 (2017).
- [21] D. González-Cuadra, E. Zohar, and J. I. Cirac, *New J. Phys.* **19**, 063038 (2017).
- [22] J. Zhang, J. Unmuth-Yockey, J. Zeiher, A. Bazavov, S.-W. Tsai, and Y. Meurice, *Phys. Rev. Lett.* **121**, 223201 (2018).
- [23] J. Unmuth-Yockey, J. Zhang, A. Bazavov, Y. Meurice, and S.-W. Tsai, *Phys. Rev. D* **98**, 094511 (2018).
- [24] J. Park, Y. Kuno, and I. Ichinose, *Phys. Rev. A* **100**, 013629 (2019).
- [25] Y. Meurice, *Phys. Rev. D* **104**, 094513 (2021).
- [26] T. Chanda, M. Lewenstein, J. Zakrzewski, and L. Tagliacozzo, *Phys. Rev. Lett.* **128**, 090601 (2022).
- [27] D. Tong, Lectures on Gauge Theory, <https://www.damtp.cam.ac.uk/user/tong/gaugetheory.html>.
- [28] Z. Komargodski, A. Sharon, R. Thorngren, and X. Zhou, *SciPost Phys.* **6**, 003 (2019).
- [29] E. Fradkin and S. H. Shenker, *Phys. Rev. D* **19**, 3682 (1979).
- [30] D. J. E. Callaway and L. J. Carson, *Phys. Rev. D* **25**, 531 (1982).
- [31] C. Gatteringer, D. Göschl, and T. Sulejmanpašić, *Nucl. Phys. B* **935**, 344 (2018).
- [32] D. Göschl, C. Gatteringer, and T. Sulejmanpasic, [arXiv:1810.09671](https://arxiv.org/abs/1810.09671).
- [33] T. Sulejmanpasic, D. Göschl, and C. Gatteringer, *Phys. Rev. Lett.* **125**, 201602 (2020).
- [34] T. Sulejmanpasic, *Phys. Rev. D* **103**, 034512 (2021).
- [35] S. Coleman, R. Jackiw, and L. Susskind, *Ann. Phys.* **93**, 267 (1975).
- [36] S. Coleman, *Ann. Phys.* **101**, 239 (1976).

- [37] T. Chanda, J. Zakrzewski, M. Lewenstein, and L. Tagliacozzo, *Phys. Rev. Lett.* **124**, 180602 (2020).
- [38] U. Schollwöck, *Ann. Phys.* **326**, 96 (2011).
- [39] R. Orús, *Ann. Phys.* **349**, 117 (2014).
- [40] M. C. Bañuls, K. Cichy, J. Cirac, and K. Jansen, *J. High Energy Phys.* **11** (2013) 158.
- [41] B. Buyens, J. Haegeman, K. Van Acoleyen, H. Verschelde, and F. Verstraete, *Phys. Rev. Lett.* **113**, 091601 (2014).
- [42] S. Kühn, J. I. Cirac, and M.-C. Bañuls, *Phys. Rev. A* **90**, 042305 (2014).
- [43] M. C. Bañuls, K. Cichy, J. I. Cirac, K. Jansen, and H. Saito, *Phys. Rev. D* **92**, 034519 (2015).
- [44] B. Buyens, F. Verstraete, and K. Van Acoleyen, *Phys. Rev. D* **94**, 085018 (2016).
- [45] T. Pichler, M. Dalmonte, E. Rico, P. Zoller, and S. Montangero, *Phys. Rev. X* **6**, 011023 (2016).
- [46] M. C. Bañuls, K. Cichy, J. I. Cirac, K. Jansen, and S. Kühn, *Phys. Rev. Lett.* **118**, 071601 (2017).
- [47] B. Buyens, J. Haegeman, H. Verschelde, F. Verstraete, and K. Van Acoleyen, *Phys. Rev. X* **6**, 041040 (2016).
- [48] G. Magnifico, M. Dalmonte, P. Facchi, S. Pascazio, F. V. Pepe, and E. Ercolessi, *Quantum* **4**, 281 (2020).
- [49] M. C. Bañuls, R. Blatt, J. Catani, A. Celi, J. I. Cirac, M. Dalmonte, L. Fallani, K. Jansen, M. Lewenstein, S. Montangero, C. A. Muschik, B. Reznik, E. Rico, L. Tagliacozzo, K. V. Acoleyen, F. Verstraete, U.-J. Wiese, M. Wingate, J. Zakrzewski, and P. Zoller, *Eur. Phys. J. D* **74**, 165 (2020).
- [50] M. Aidelburger, L. Barbiero, A. Bermudez, T. Chanda, A. Dauphin, D. González-Cuadra, P. R. Grzybowski, S. Hands, F. Jendrzejewski, J. Jünemann, G. Juzeliūnas, V. Kasper, A. Piga, S.-J. Ran, M. Rizzi, G. Sierra, L. Tagliacozzo, E. Tirrito, T. V. Zache, J. Zakrzewski *et al.*, and *Philos. Trans. R. Soc. A* **380** (2021).
- [51] J. Schwinger, *Phys. Rev.* **82**, 664 (1951).
- [52] S. R. White, *Phys. Rev. Lett.* **69**, 2863 (1992).
- [53] S. R. White, *Phys. Rev. B* **48**, 10345 (1993).
- [54] S. R. White, *Phys. Rev. B* **72**, 180403(R) (2005).
- [55] U. Schollwöck, *Rev. Mod. Phys.* **77**, 259 (2005).
- [56] J. Haegeman, J. I. Cirac, T. J. Osborne, I. Pižorn, H. Verschelde, and F. Verstraete, *Phys. Rev. Lett.* **107**, 070601 (2011).
- [57] J. Haegeman, C. Lubich, I. Oseledets, B. Vandereycken, and F. Verstraete, *Phys. Rev. B* **94**, 165116 (2016).
- [58] T. Koffel, M. Lewenstein, and L. Tagliacozzo, *Phys. Rev. Lett.* **109**, 267203 (2012).
- [59] S. Paeckel, T. Köhler, A. Swoboda, S. R. Manmana, U. Schollwöck, and C. Hubig, *Ann. Phys.* **411**, 167998 (2019).
- [60] H. W. J. Blöte, J. L. Cardy, and M. P. Nightingale, *Phys. Rev. Lett.* **56**, 742 (1986).
- [61] I. Affleck, *Phys. Rev. Lett.* **56**, 746 (1986).
- [62] I. Affleck, D. Gepner, H. J. Schulz, and T. Ziman, *J. Phys. A* **22**, 511 (1989).
- [63] K. Hallberg, X. Q. G. Wang, P. Horsch, and A. Moreo, *Phys. Rev. Lett.* **76**, 4955 (1996).
- [64] J. C. Xavier, *Phys. Rev. B* **81**, 224404 (2010).
- [65] M. Dalmonte, E. Ercolessi, and L. Taddia, *Phys. Rev. B* **85**, 165112 (2012).
- [66] N. Chepiga and F. Mila, *Phys. Rev. B* **96**, 054425 (2017).
- [67] S. Singh, R. N. C. Pfeifer, and G. Vidal, *Phys. Rev. A* **82**, 050301(R) (2010).
- [68] S. Singh, R. N. C. Pfeifer, and G. Vidal, *Phys. Rev. B* **83**, 115125 (2011).
- [69] H. Casini, M. Huerta, and J. A. Rosabal, *Phys. Rev. D* **89**, 085012 (2014).
- [70] S. Ghosh, R. M. Soni, and S. P. Trivedi, *J. High Energy Phys.* **09** (2015) 069.
- [71] R. M. Soni and S. P. Trivedi, *J. High Energy Phys.* **01** (2016) 136.
- [72] C. Callan and F. Wilczek, *Phys. Lett. B* **333**, 55 (1994).
- [73] G. Vidal, J. I. Latorre, E. Rico, and A. Kitaev, *Phys. Rev. Lett.* **90**, 227902 (2003).
- [74] P. Calabrese and J. Cardy, *J. Stat. Mech.* (2004) P06002.
- [75] J. Cardy and P. Calabrese, *J. Stat. Mech.* (2010) P04023.
- [76] E. Eriksson and H. Johannesson, *J. Stat. Mech.* (2011) P02008.
- [77] N. Laflorencie, E. S. Sørensen, M.-S. Chang, and I. Affleck, *Phys. Rev. Lett.* **96**, 100603 (2006).
- [78] J. L. Cardy, *Nucl. Phys. B* **275**, 200 (1986).
- [79] J. L. Cardy, *Nucl. Phys. B* **270**, 186 (1986).
- [80] A. Rocha-Caridi, *Mathematical Sciences Research Institute Publications* (Springer, US, 1985), pp. 451–473.
- [81] G. Evenbly and G. Vidal, *J. Stat. Phys.* **157**, 931 (2014).
- [82] T. Giamarchi, *Quantum Physics in One Dimension*, International Series of Monographs on Physics (Oxford University Press, Oxford, 2003).
- [83] A. O. Gogolin, A. A. Nersisyan, and A. M. Tsvelik, *Bosonization and Strongly Correlated Systems* (Cambridge University Press, Cambridge, England, 2004).
- [84] H. F. Song, S. Rachel, and K. Le Hur, *Phys. Rev. B* **82**, 012405 (2010).
- [85] H. F. Song, S. Rachel, C. Flindt, I. Klich, N. Laflorencie, and K. Le Hur, *Phys. Rev. B* **85**, 035409 (2012).
- [86] S. Rachel, N. Laflorencie, H. F. Song, and K. Le Hur, *Phys. Rev. Lett.* **108**, 116401 (2012).
- [87] L. Villa, J. Despres, and L. Sanchez-Palencia, *Phys. Rev. A* **100**, 063632 (2019).
- [88] L. Villa, J. Despres, S. J. Thomson, and L. Sanchez-Palencia, *Phys. Rev. A* **102**, 033337 (2020).
- [89] M. Fishman, S. R. White, and E. M. Stoudenmire, *SciPost Phys. Codebases* **4** (2022).
- [90] M. Fishman, S. R. White, and E. M. Stoudenmire, *SciPost Phys. Codebases* **4-r0.3** (2022).
- [91] C. Hubig, I. P. McCulloch, U. Schollwöck, and F. A. Wolf, *Phys. Rev. B* **91**, 155115 (2015).